Origin of spontaneous wave mixing processes in multimode GRIN fibers

A. Bendahmane, M. Conforti, O. Vanvincq, C. Mas Arabí, A. Mussot, A. Kudlinski

Research Article | Vol. 29, No. 19 / 13 Sep 2021 / Optics Express 30822
Optics EXPRESS

Origin of spontaneous wave mixing processes in multimode GRIN fibers

A. Bendahmane,[1,2] M. Conforti,[1] O. Vanvincq,[1] C. Mas Arabí,[1,3] A. Mussot,[1] and A. Kudlinski[1,*]

[1] *Univ. Lille, CNRS, UMR 8523 - PhLAM - Physique des Lasers Atomes et Molécules, F- 59000 Lille, France*
[2] *Currently with Emergent Photonics (Epic) Laboratory, Department of Physics and Astronomy, University of Sussex, Brighton, UK*
[3] *Currently with Service OPERA-photonics, Université libre de Bruxelles, 50 Avenue F. D. Roosevelt, CP 194/5, B- 1050 Bruxelles, Belgium*
[*] *alexandre.kudlinski@univ-lille.fr*

Abstract: We show that geometric parametric instability (GPI) in graded-index multimode fibers is strongly influenced by higher-order dispersion. By measuring the output spectrum for different core radii, we distinguish peaks generated by GPI from other coexisting parametric processes using phase-matching arguments and numerical simulations. We highlight for the first time a non-degenerate GPI process involving two pumps at different wavelengths.

1. Introduction

Graded-index (GRIN) multimode optical fibers (MMFs) were developed historically to reduce modal dispersion in first-generation multimode optical communication systems [1,2] in the seventies. One of their main characteristics is that the propagation constants of the modes are equally spaced, which provides a periodic focalisation of the overall field in the core, known as self-imaging [3,4]. Three decades later, it was shown theoretically that this periodic self-imaging process could induce a refractive index grating through the Kerr effect, allowing parametric instability to take place [5].

After pioneering experimental studies in the eighties [6], there has been a strong renew of interest in nonlinear optics in GRIN MMFs over the last ten years [7–10], with the observation of multimode spatiotemporal solitons [11,12], supercontinuum generation [13–15], geometric parametric instability (GPI) [16–19] and beam self-cleaning [20,21]. The role of the Kerr-induced refractive index grating has been unambiguously identified in several of these experimental works, including the emission of quasi-phase matched radiations from solitons [22] and the observation of GPI [16].

GPI has been extensively studied experimentally in GRIN MMFs since its first observation in 2016 [16]. It can be described either by using the collective approach initially developed by Longhi [5] in which the evolution of the total field in the fiber is considered, or by intermodal four-wave mixing (FWM) processes. In this last case, multiple quasi-phase-matched (QPM) processes assisted by the Kerr-induced refractive index grating of individual modes are considered [23]. It is now well accepted in the literature that both approaches are equivalent and constitute two different ways of describing the same phenomenon. Although GPI has been clearly observed many times [16,17,24–27], many other FWM processes can coexist with GPI in a GRIN MMF depending on the fiber parameters, such as intermodal FWM [23,28], non-degenerate FWM between the pump and the first GPI band [24,28], or cascaded FWM of the first GPI band [24]. This makes experimental spectra very rich and complex and it is often tricky to unambiguously identify the generated sidebands and their underlying mechanism.

#436229 https://doi.org/10.1364/OE.436229
Journal © 2021 Received 13 Jul 2021; revised 25 Aug 2021; accepted 25 Aug 2021; published 9 Sep 2021

Optics EXPRESS

In this work, we show that higher-order dispersion (HOD) (which is often disregarded in the analysis) plays a crucial role in the GPI process as it is responsible for additional sideband pairs. We also demonstrate that up to four different parametric processes can take place simultaneously in typical GPI experiments, among which an unprecedented non-degenerate GPI process involving two pumps is identified. We provide a physical interpretation of the multi-line spectra through a careful comparison between theory, numerical simulations and experiments.

2. Impact of higher dispersion terms on the GPI process

The GPI process in GRIN MMFs is possible thanks to the Kerr-induced refractive index grating created by the periodic self-imaging of the beam with a spatial period $Z = \pi R/\sqrt{2\Delta}$, where R is the fiber core radius and $\Delta = (n_{\text{core}}^2 - n_{\text{clad}}^2)/2n_{\text{core}}^2$ is the relative index difference (n_{core} is the refractive index at the center of the core and n_{clad} is the one of the cladding). It can be analyzed using the following general QPM relation [16]:

$$\beta_e(\Omega) + \overline{\gamma}P = k\pi/Z \tag{1}$$

where $\beta_e(\Omega) = \sum_{n\geq 1} \frac{\beta_{2n}}{(2n)!}\Omega^{2n}$ is the even part of the dispersion operator (with $\Omega = \omega - \omega_0$ and ω_0 the pump frequency), P is the pump power and k is an integer. $\overline{\gamma}$ is the nonlinear parameter averaged over the fiber length, as defined in [29]. This kind of QPM process is analogue to QPM processes induced by periodic dispersion or power in long-haul telecommunation systems [30–33] or in dispersion oscillating fibers [34–36].

Usually, only second-order dispersion β_2 (corresponding to $n = 1$) is considered in the analysis of GPI using Eq. (1). However, it has been demonstrated in dispersion oscillating fibers that the impact of HOD may be significant for specific parameter ranges in similar parametric QPM processes, even relatively far from the zero dispersion wavelength [37]. The GPI process was analyzed using the full dispersion curve in Ref. [25], but no specific features due to HOD were highlighted in the range of parameters investigated in that study. Also, the role of fourth-order dispersion was highlighted in [26] and its impact on the GPI process was found to be quite small in the case of large core GRIN MMFs (R>50 μm). It is therefore natural to investigate its impact on the GPI process more deeply than in Ref. [38], in conventional commercially available GRIN MMFs with smaller cores. To do that, we calculate the roots of Eq. (1) by considering second and fourth-order dispersion (*i.e.* $n = 2$) and neglecting the nonlinear phase mismatch [23]. We obtain the following expression for the roots of Eq. (1) [26]:

$$\Omega_k^2 = \frac{-6\beta_2}{\beta_4} \pm \sqrt{\left(\frac{6\beta_2}{\beta_4}\right)^2 + \frac{24k\sqrt{2\Delta}}{R\beta_4}} \tag{2}$$

Equation (2) shows that for each value of the integer k, two sideband pairs are theoretically obtained, while only one sideband pair per k value is obtained when the dispersion order is limited to 2 [38]. To illustrate this more clearly, we plot in Fig. 1 solutions from Eq. (2) as a function of core radius R, for $k = 1$ to 3. We plot here the relative frequency to the pump laser $\Delta f = \Omega/2\pi$, as in the rest of the paper. Red solid lines are plotted when taking into account both second and fourth-order dispersion, while blue dashed lines correspond to the case where only second-order dispersion is considered. For this school case of study, we consider a fiber with $\Delta = 0.025$ and we use the dispersion parameters of pure silica from Ref. [39] (see Fig. 1 caption). This is equivalent to neglecting the contribution of the Ge content in the core to the overall glass dispersion. Although this is realistic for GRIN MMFs in first approximation, we shall see in the following sections that more care must be taken to estimate the dispersion in the perspective of making a quantitative comparison with experiments.

Two main conclusions can be drawn from these plots. First, for each value of k, two solutions appear (on both sides of the pump) for a given core radius when β_4 is taken into account, while

Optics EXPRESS

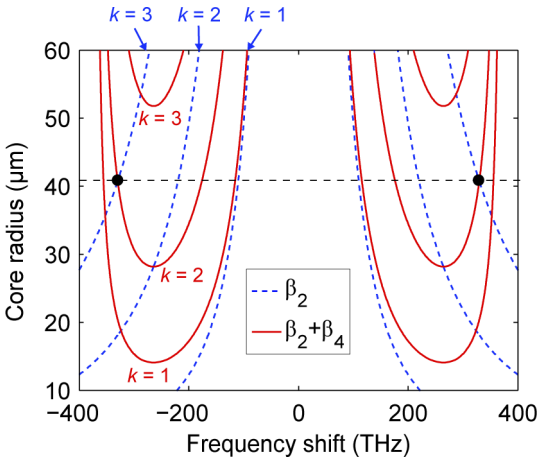

Fig. 1. Frequency shift of GPI sidebands as a function of fiber core radius plotted from Eq. (2) for the first three orders (for $k = 1$ to 3) when both second and fourth-order dispersion are considered (red solid lines) and when fourth-order dispersion is neglected (blue dashed lines). Parameters : $\Delta = 0.025$, $\beta_2 = 23 \times 10^{-27}$ s^2.m^{-1} and $\beta_4 = -5 \times 10^{-56}$ s^4.m^{-1}. The horizontal black dashed line and black dots correspond to the $R = 41$ μm example discussed in the text.

there is only one when only β_2 is considered, as discussed above with Eq. (2). This is an important feature to take into account when trying to interpret the origin of all sidebands observed in experimental spectra : for instance, for a core radius of 41 μm (depicted by the horizontal black dashed line), a frequency shift of ± 330 THz would be interpreted as the $k = 3$ sideband by neglecting β_4 (blue dashed curve), while it is actually due to the second branch of the $k = 2$ order (red solid line), as depicted by black dots in Fig. 1.

Second, there is a core radius value (of about 15 μm) under which no GPI can be observed when β_4 is taken into account. This threshold does not exist when only second order dispersion is considered.

Our aim in the following is to observe experimentally the impact of HOD on the GPI process and to identify all generated peaks with a quantitative agreement with QPM theory. As discussed above, taking fourth-order dispersion into account is sufficient to highlight the basic features due to HOD as we did in this section, but in view of getting a quantitative agreement with experiments, the whole dispersion curves will be taken into account in the following. It is therefore crucial to know the dispersion properties of the fiber core as accurately as possible.

3. Choice of the refractive index dispersion model

The core of GRIN MMFs is usually made of GeO_2-doped silica glass. Their refractive index profile can be easily measured at a fixed wavelength using commercial refractive index profilometers. However, one needs to know accurately the dispersion of the core material in the present study, in order to solve numerically Eq. (1).

In the following analytical results, we assume that the dispersion of the lowest order modes involved in the GPI process is equal to that of silica doped with the maximal Ge content of the fiber. This is in fact only valid far from cut-off wavelengths of the modes but we have checked with a finite difference mode solver that this is true for modes up to $LP_{0,7}$ when the wavelength is less than 2 μm.

One can find several models in the literature to calculate the dispersion of GeO_2 glasses : the Fleming [40] and Okamoto [41] models are an interpolation of Sellmeier coefficients with

Optics EXPRESS

Ge content and the Sunak model uses a Claussius-Mossotti interpolation scheme to obtain the refractive index of germanosilicate glasses [42]. In order to select the most appropriate one, we will confront the roots of Eq. (1) obtained with each of these models with the position of the $k = 1$ GPI sideband experimentally observed in standard GRIN MMFs. We focus our study on the first GPI sideband because it is the only one which can be usually identified with no ambiguity in most experiments thanks to its strong parametric gain.

These preliminary experiments were done using two commercial MMFs from Prysmian, labeled OM1 and OM2. Fiber OM1 has a core radius of 32.5 μm and a Δ parameter of 0.0188 and fiber OM2 has a core radius of 26 μm and a Δ parameter of 0.0088. These parameters were obtained from the measurement of their refractive index profile done at 976 nm with a commercial profilometer (not shown here).

The fiber length is 1.2 m and they are pumped with a powerchip laser at 1064 nm delivering 500 ps pulses at 1 kHz. The radius of the focal spot on the fiber input face is 6 μm. Figures 2(a) and (b) show the spectrum of the $k = 1$ GPI sideband (black line) measured respectively in fiber OM1 and OM2, for an input peak power of 60 kW. Blue, red and green vertical lines represent the root of Eq. (1) obtained for $k = 1$, respectively with the dispersion model from Okamoto [41], Sunak [42] and Fleming [40] with a Ge content of 18 mol.% for fiber OM1 and 8.3 mol.% for fiber OM2. All models give relatively close results to our experiments, since the maximal discrepancy with experiments does not exceed 7 % as can be seen from Table 1 summarizing these results. However, the Sunak model clearly gives the closest results to our experiments, with a 0.5 % accuracy. We will therefore use the Sunak model [42] in what follows for the analysis of experimental results.

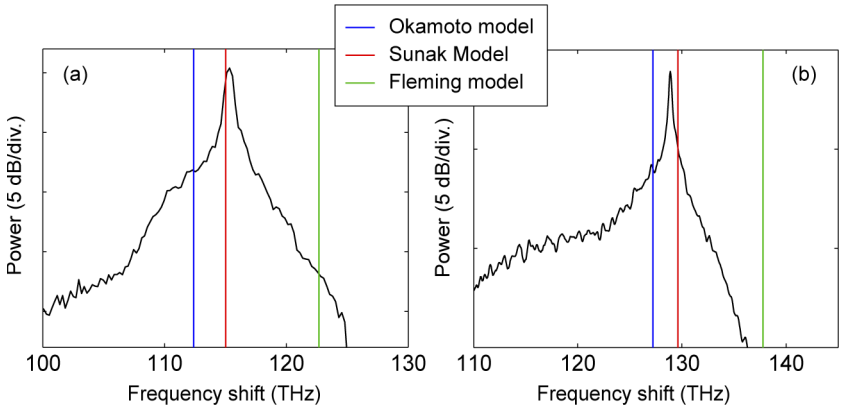

Fig. 2. First order ($k = 1$) GPI spectra measured in (a) OM1 and (b) OM2 GRIN MMFs (black lines). Blue, red and green vertical lines correspond to roots of Eq. (1) obtained respectively with the models from Okamoto [41], Sunak [42] and Fleming [40].

Table 1. Summary of the results from Fig. 2.

R (μm)	Δf_1 (THz) Experiments	Δf_1 (THz) Okamoto model [41]	Δf_1 (THz) Sunak model [42]	Δf_1 (THz) Fleming model [40]
26	128.9	127.2	129.6	137.8
32.5	115.4	112.4	115.0	122.7

Optics EXPRESS

4. Origin of parametric processes

Our aim in this section is to identify the origin of multiple peaks observed in GPI experiments and in particular to highlight specific features arising from HOD in two reference commercial GRIN MMFs.

4.1. Quasi-phase-matching diagrams

We start by studying the QPM diagrams for fibers OM1 and OM2 described above, by solving numerically Eq. (1). To do that, we use the full dispersion curves obtained from the Sunak model with appropriate Ge content of 18 mol.% and 8.3 mol.% respectively for fibers OM1 and OM2. Other parameters are the same as in the previous section. We focus here on the positive frequency detuning part, since the short wavelength side of the pump is usually more easily accessible in experiments. The negative detuning part is symmetric with respect to the pump frequency.

The QPM diagrams calculated for fibers OM1 and OM2 respectively are displayed in Fig. 3(a) and (b), for core radii R varying from 10 to 80 μm and for k values ranging from -2 to 3. In the frequency range of interest, positive k values give two solutions. However, it must be noticed that for both core radii depicted by the horizontal dashed lines, two $k = 1$ solutions are possible but solutions corresponding to $k \geq 2$ values are not expected to be observed.

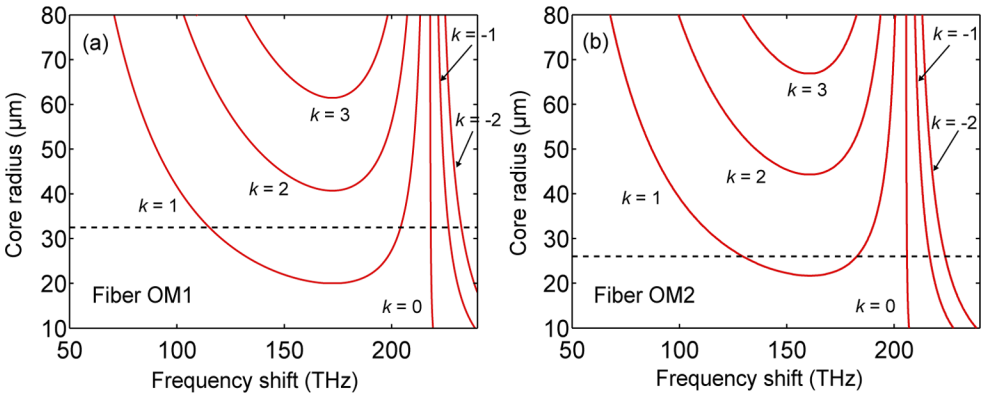

Fig. 3. QPM diagrams obtained from Eq. (1) (see details in the text), for GRIN fibers (a) OM1 and (b) OM2. Horizontal black dashed lines represent the core radius of each corresponding fiber.

$k \leq 0$ values give one solution with a very large frequency shift >200 THz. Using a typical 1064 nm pump, the large negative frequency detuning associated to the Stokes sideband corresponds to infrared wavelengths beyond 3000 nm, for which germanium-doped silica glasses strongly absorb [43], which affects the GPI process and the generation symmetric sidebands with respect to the pump. Additionally, some of higher-order modes contributing to the GPI process have their cutoff in this wavelength region, which kills the generation of GPI sidebands. Experimentally, GPI sidebands corresponding to frequency shift >190 THz are not observed for those reasons. The sidebands observed at larger frequency shifts have a different origin, as we shall see in the following.

4.2. Cascaded GPI

Most of typical GPI experiments usually show the generation of more new frequencies than predicted by Eq. (1). This means that additional nonlinear mechanisms are involved, among which the *cascaded* GPI process plays a central role [24]. In this process, the pump laser generates a $k = 1$ GPI anti-Stokes sideband which is intense enough to act as a secondary pump then

Optics EXPRESS

generating its own GPI process. This cascaded GPI process is at the origin of multiple visible sidebands [24]. Figures 4(a) and (b) illustrates this for fibers OM1 and OM2, respectively. Red lines correspond to the roots of Eq. (1) obtained from the pump laser with a peak power of 60 kW, truncated at 190 THz beyond which the sidebands are not observed as discussed above. In fiber OM1 (Fig. 4(a)), the second branch of the $k = 1$ GPI sideband, which is due to HOD, is not expected to be observed because it would be located well beyond 190 THz. However, it should be observed in fiber OM2, since it falls around 180 THz, as can be seen from 4(b). Let us recall that in both fibers, $k \geq 2$ GPI sidebands are not expected to be observed for core radii corresponding to fibers OM1 and OM2.

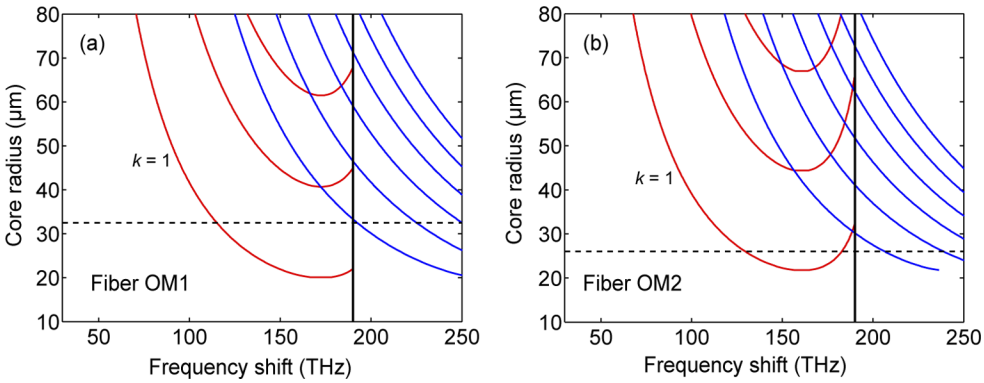

Fig. 4. GPI phase-matching diagrams obtained with Eq. (1) from the pump laser (red lines) and from the $k = 1$ sideband (blue lines), corresponding to the cascaded GPI process, for GRIN fibers (a) OM1 and (b) OM2. Horizontal black dashed lines represent the core radius of each corresponding fiber. Vertical solid black lines represents the 190 THz limit beyond which primary GPI is neglected (see details in text).

Blue lines in Figs. 4(a) and (b) correspond to the cascaded GPI process generated from the $k = 1$ sideband acting as a secondary pump of 30 kW (located at 115 THz for fiber OM1 and around 130 THz for fiber OM2) but plotted here relatively to the pump wavelength. Note that in this case, they can be observed beyond the 190 THz line (black vertical line), because their relative frequency shift to the secondary pump (located on the short wavelength side) is much less since no GPI bands associated to the secondary pump fall inside the wavelength region with a strong absorption.

5. Experimental investigation

In this section, we will use the results of phase-matching diagrams plotted in Fig. 4 to analyze complex experimental spectra and identify the origin of all peaks, with further support from numerical simulations.

We performed experiments with the two commercial fibers OM1 and OM2 described in section 3 with the same experimental setup. Numerical simulations were done using a multimode generalized nonlinear Schrödinger equation (MGNLSE) model described in Appendix A.

5.1. Fiber OM1

Figure 5(a) shows the experimental spectrum measured in a fiber length of 1.2 m for a pump peak power of 60 kW. We have also represented the theoretical GPI frequency (vertical red dashed line) and cascaded GPI (vertical blue dashed lines) with corresponding k values. Here we observe an intense $k = 1$ GPI peak at 115 THz, a cascaded GPI peak of order 2 at 222 THz, and several

Optics EXPRESS

other peaks not corresponding to GPI nor cascaded GPI. We have therefore considered additional nonlinear processes.

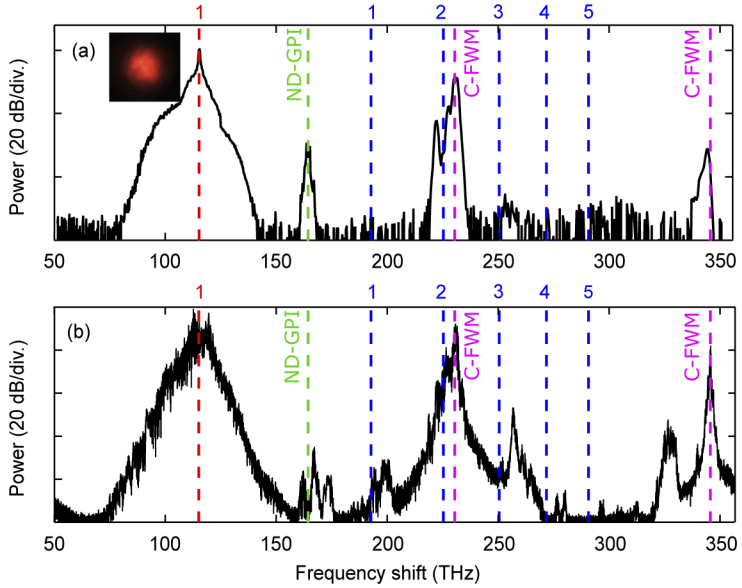

Fig. 5. (a) Experimental and (b) simulated spectrum in 1.2 m of fiber OM1. Red dashed lines: GPI obtained from Eq. (1). Blue dashed lines: cascaded GPI generated from the main GPI sideband ($k = 1$) at 115 THz. Magenta dashed lines: harmonics of the main GPI sideband ($k = 1$). Green dashed lines: non-degenerate GPI involving the pump laser and the main GPI sideband. The inset shows the experimental near field profile of the $k = 1$ sideband.

The first one is a degenerate cascaded FWM (labeled C-FWM, vertical magenta dashed lines), corresponding to harmonics of the $k = 1$ GPI sideband, thus occurring at twice and three times the frequency shift of the first GPI sideband. This process explains the relatively intense peaks observed at 230 and 345 THz in Fig. 5(a). Note that the 230 THz C-FWM peak probably acts as a seed for the generation of the $k = 2$ cascaded GPI peak at 222 THz [26], which could explain why only the $k = 2$ peak is observed, and not the other ones.

The second additional process we have to take into account to explain the remaining 165 THz peak is a non-degenerate GPI involving the pump laser and the first GPI sideband (labeled ND-GPI, vertical green dashed lines). It obeys the following QPM relation (neglecting the nonlinear phase mismatch) :

$$\beta_{\mathrm{A}} + \beta_{\mathrm{S}} - \beta_{\mathrm{P1}} - \beta_{\mathrm{P2}} = 2k'\pi/Z \tag{3}$$

where β_A and β_S are the propagation constants of the anti-Stokes and Stokes components, β_{P1} and β_{P2} are the ones of the two pumps and k' is an integer. This is a two-pump GPI process which can also be interpreted as an intermodal FWM introduced in [23]. For our experimental results of Fig. 5(a), the two pumps of the process are the main pump laser (1064 nm) and the $k = 1$ GPI sideband (755 nm). From Eq. (3), we obtain a frequency shift of 165 THz for the anti-Stokes component (with $k' = 1$), which is in excellent agreement with the experimental peak.

Corresponding numerical simulations represented in Fig. 5(b) are in excellent agreement. They confirm the presence of a strong first-order GPI peak at 115 THz and of the cascaded FWM peaks at twice and three times this frequency shift. The non-degenerate GPI peak located at 165 Thz is also observed in simulations, also it appears less clear than in experiments. Simulations

Optics EXPRESS

also confirms that cascaded GPI orders different than 2 are not observed, as discussed above. Finally, simulations show additional weak peaks (around 260 THz and 330 Thz) which are not observed in measurements probably to the higher experimental noise floor.

5.2. Fiber OM2

Figures 6(a) and (b) show respectively the experimental and simulated spectrum in 1.2 m of fiber OM2, for a peak power of 60 kW. Vertical dashed lines follow the same representation as in Fig. 5. As expected from phase matching diagrams for this fiber, the two GPI solutions corresponding to $k = 1$ are observed at 127 and 182 THz in good agreement with the phase matching results of Fig. 4(b), which highlights the importance of taking HOD into account. Additionally, several cascaded GPI sidebands are observed, corresponding to orders -1, 1, 2 and 3. An harmonic of the first GPI sideband is also observed (in magenta) very close to the third order cascaded GPI sideband. The 89 THz experimental peak is a residue of the 808 nm pump diode of the 1064 nm laser. Non-degenerate GPI sidebands are not observed in this experiment so their corresponding theoretical frequency is not represented. Again, the simulated spectrum is in excellent agreement with experiments and confirms the origin of the peaks experimentally observed.

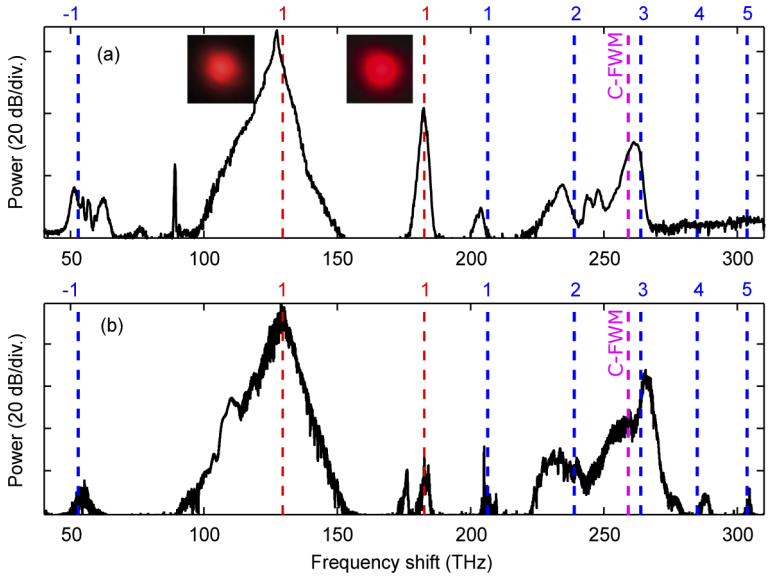

Fig. 6. (a) Experimental and (b) simulated spectrum in 1.2 m of fiber OM2. Red dashed lines: GPI obtained from Eq. (1). Blue dashed lines: cascaded GPI generated from the main GPI sideband ($k = 1$) at 115 THz. Magenta dashed lines: harmonics of the main GPI sideband ($k = 1$). The inset shows the experimental near field profiles of the two $k = 1$ sidebands.

5.3. Few mode GRIN fiber

In this section, we propose an alternative interpretation of previously published experimental results of Ref. [24], based on our theoretical analysis of Section 4. These results were obtained in a $R = 11$ μm core GRIN MMF, with $\Delta = 0.0089$. Full details about the setup and the fiber can be found in Ref. [24]. Figure 7(a) shows roots of Eq. (1) obtained for $k = 0, 1$ and 2 (red lines). The horizontal black dashed line represents the core radius of 11 μm, showing that for this specific fiber, $k = 1, 2$ GPI sidebands (due to the periodic Kerr grating) are not expected to be observed. Only the $k = 0$ root (not involving the Kerr grating) is expected to be observed

Optics EXPRESS

close to 200 THz. Blue lines correspond to cascaded GPI from this $k = 0$ sideband acting as a secondary pump when it becomes intense enough.

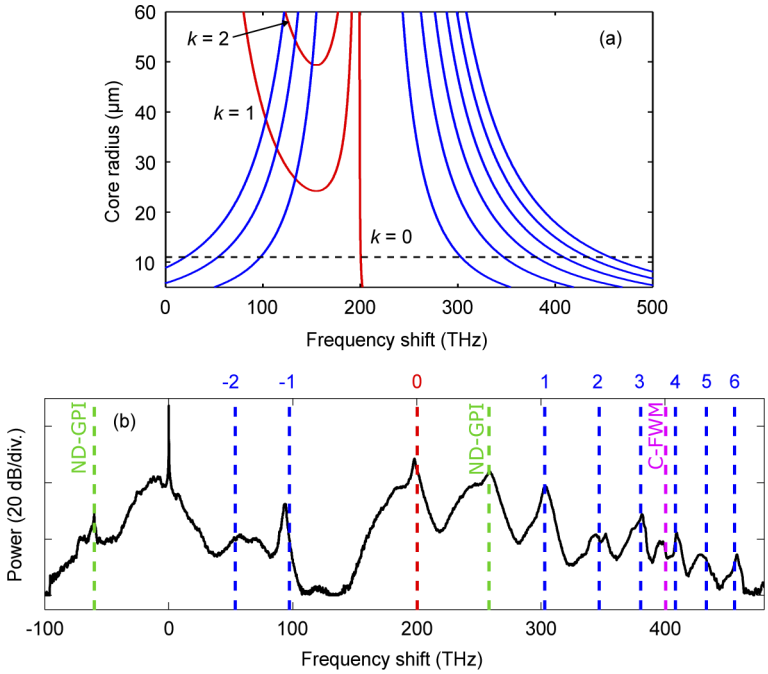

Fig. 7. (a) GPI QPM diagrams obtained with Eq. (1) from the pump laser (red lines) and from the $k = 0$ sideband (blue lines), corresponding to the cascaded GPI process, in the few mode fiber of Ref. [24]. Horizontal black dashed lines represent the $R = 11$ μm core radius. (b) Experimental spectrum adapted from Fig. 2(a) of Ref. [24] (black line). Red dashed lines: GPI obtained from Eq. (1). Blue dashed lines: cascaded GPI generated from the main GPI sideband ($k = 0$) at about 200 THz. Magenta dashed lines: harmonics of the main GPI sideband ($k = 0$). Green dashed lines: non-degenerate GPI involving the pump laser and the $k = 0$ sideband.

Figure 7(b) shows the experimental spectrum plotted with the data corresponding to the black line of Fig. 2(a) of Ref. [24]. We have superimposed theoretical frequencies corresponding to the $k = 0$ root (red dashed line) and to the cascaded GPI of order -2 to 6 generated from this $k = 0$ main band (dashed blue) lines. All experimental peaks are in excellent agreement with our analysis, highlighting the fact that taking HOD into account provides an alternative interpretation of experimental results. A cascaded FWM process is observed very close to 400 THz (magenta dashed line). Additional experimental peaks are in excellent agreement with the non-degenerate GPI process described above by Eq. (3), with the two pumps being this time the main pump laser and the $k = 0$ sideband located at 198 THz. The Stokes and anti-Stokes roots of Eq. (3) located respectively at -60 and 258 THz (represented by green dashed lines) are in excellent agreement with experimental peaks.

6. Summary and discussion

Several important conclusions can be drawn from these experiments. First, taking HOD into account has a very significant impact on the phase-matching diagram of GPI sidebands. In the two commercially available fibers, only the first order of the GPI sidebands can be observed ($k = 1$). Depending on the fiber parameters, one or two $k = 1$ branches can be observed (respectively

Optics EXPRESS

in fiber OM1 and OM2). In the second case, the second branch of the $k = 1$ GPI is a specific feature due to HOD, which is not seen in the analysis when HOD is neglected. Here, we have been able to observe and interpret it unambiguously. In the few mode GRIN fiber, our analysis reveals that GPI induced by the periodic Kerr grating due to periodic self-imaging ($k \neq 0$) cannot be observed, but instead, only the $k = 0$ root is observable as the main process.

Second, depending again on fiber parameters, several other nonlinear processes may occur when the main GPI sideband is powerful enough, and generate additional sidebands. They include (i) cascaded GPI from the $k = 1$ GPI sideband in MMFs or from the $k = 0$ one in the few mode fiber [24] (which therefore act as a secondary pump), (ii) cascaded degenerate FWM (harmonics of the $k = 1$ or $k = 0$ GPI sideband, depending on the fiber) and (iii) non degenerate GPI involving the pump and the $k = 1$ GPI sideband (or the $k = 0$ one in the few mode fiber).

Of course, the agreement between phase-matching arguments and experiments strongly relies on the choice of the dispersion model used for the Ge-doped glass in the core, as discussed in Section 3. Here we found that the Sunak model gives the best agreement with our experiments, but we have no physical arguments to justify this choice. Note however that although other models would gives less quantitative agreement with experiments, they would not change the interpretation about the origin of the nonlinear mechanisms.

To conclude, we showed that experimental GPI spectra are often very rich and their interpretation using phase-matching arguments is not as straightforward as it may look at first view because many parametric processes coexist. We have shown in particular that taking higher-order dispersion into account is crucial for the analysis of experimental results. We have also identified experimentally for the first time a non-degenerate GPI process involving two pumps. Further analysis would require to take into account the overlap integral of the modes involved in various wave mixing processes in order to explain why some specific k^{th} order sidebands are weaker than other (or sometimes not observed).

Appendix A: MGNLSE model

The numerical results were obtained by solving the MGNLSE introduced by Afshar and Monro [44]. Assuming a centered injection of the light in the fiber, we only considered the $LP_{0,j}$ modes ($j \leq 8$ for fiber OM2 and $j \leq 14$ for fiber OM1). The dispersion of the modes was computed with a finite difference method applied on the refractive index profile measured with a commercial refractive index profilometer and by taking into account the dispersion of the Ge-doped silica given by Sunak [42]. The nonlinear overlap integrals were computed at the pump wavelength and assumed to be independent of the wavelength. Silica losses and cut-off wavelengths of the modes were also taken into account. We used the RK4IP method [45] implemented on GPU with a constant step of 2 μm to solve the MGNLSE.

Funding. Contrat de Projets État-Région; European Regional Development (HEAFISY); Nord-Pas-de-Calais Regional Council (HEAFISY); Agence Nationale de la Recherche (ANR-11-LABX-0007-01, ANR-16-IDEX-0004).

Acknowledgements. We acknowledge Prysmian Group (Parc Ind Artois Flandres, 62092 Haisnes, France) for the loan of GRIN MMFs and Guy Millot (Université Bourgogne Franche-Comté, ICB UMR CNRS 6303, 21078 Dijon, France) for providing data from the experimental measurements of Fig. 7(b).

Disclosures. The authors declare no conflicts of interest.

Data availability. Data underlying the results presented in this paper may be obtained from the authors upon reasonable request.

Optics EXPRESS

References

1. T. Uchida, M. Furukawa, I. Kitano, K. Koizumi, and H. Matsumura, "Optical characteristics of a light-focusing fiber guide and its applications," IEEE J. Quantum Electron. **6**(10), 606–612 (1970).
2. G. P. Agrawal, A. K. Ghatak, and C. L. Mehta, "Propagation of a partially coherent beam through Selfoc fibers," Opt. Commun. **12**(3), 333–337 (1974).
3. D. Gloge and E. A. J. Marcatili, "Multimode theory of graded-core fibers," The Bell Syst. Tech. J. **52**(9), 1563–1578 (1973).
4. A. Mafi, "Pulse Propagation in a Short Nonlinear Graded-Index Multimode Optical Fiber," J. Lightwave Technol. **30**(17), 2803–2811 (2012).
5. S. Longhi, "Modulational instability and space time dynamics in nonlinear parabolic-index optical fibers," Opt. Lett. **28**(23), 2363–2365 (2003).
6. K. O. Hill, D. C. Johnson, and B. S. Kawasaki, "Efficient conversion of light over a wide spectral range by four-photon mixing in a multimode graded-index fiber," Appl. Opt. **20**(6), 1075–1079 (1981).
7. L. G. Wright, W. H. Renninger, D. N. Christodoulides, and F. W. Wise, "Spatiotemporal dynamics of multimode optical solitons," Opt. Express **23**(3), 3492–3506 (2015).
8. L. G. Wright, D. N. Christodoulides, and F. W. Wise, "Controllable spatiotemporal nonlinear effects in multimode fibres," Nat. Photonics **9**(5), 306–310 (2015).
9. G. P. Agrawal, "Invite paper: Self-imaging in multimode graded-index fibers and its impact on the nonlinear phenomena," Opt. Fiber Technol. **50**, 309–316 (2019).
10. P. Mondal, V. Mishra, and S. K. Varshney, "Nonlinear interactions in multimode optical fibers," Opt. Fiber Technol. **54**, 102041 (2020).
11. W. H. Renninger and F. W. Wise, "Optical solitons in graded-index multimode fibres," Nat. Commun. **4**(1), 1719 (2013).
12. L. G. Wright, Z. Liu, D. A. Nolan, M.-J. Li, D. N. Christodoulides, and F. W. Wise, "Self-organized instability in graded-index multimode fibres," Nat. Photonics **10**(12), 771–776 (2016).
13. G. Lopez-Galmiche, Z. S. Eznaveh, M. A. Eftekhar, J. A. Lopez, L. G. Wright, F. Wise, D. Christodoulides, and R. A. Correa, "Visible supercontinuum generation in a graded index multimode fiber pumped at 1064 nm," Opt. Lett. **41**(11), 2553–2556 (2016).
14. M. A. Eftekhar, L. G. Wright, M. S. Mills, M. Kolesik, R. A. Correa, F. W. Wise, and D. N. Christodoulides, "Versatile supercontinuum generation in parabolic multimode optical fibers," Opt. Express **25**(8), 9078–9087 (2017).
15. S. Perret, G. Fanjoux, L. Bigot, J. Fatome, G. Millot, J. M. Dudley, and T. Sylvestre, "Supercontinuum generation by intermodal four-wave mixing in a step-index few-mode fibre," APL Photonics **4**(2), 022905 (2019).
16. K. Krupa, A. Tonello, A. Barthélémy, V. Couderc, B. M. Shalaby, A. Bendahmane, G. Millot, and S. Wabnitz, "Observation of Geometric Parametric Instability Induced by the Periodic Spatial Self-Imaging of Multimode Waves," Phys. Rev. Lett. **116**(18), 183901 (2016).
17. Z. S. Eznaveh, M. A. Eftekhar, J. E. A. Lopez, M. Kolesik, A. Schülzgen, F. W. Wise, D. N. Christodoulides, and R. A. Correa, "Tailoring frequency generation in uniform and concatenated multimode fibers," Opt. Lett. **42**(5), 1015–1018 (2017).
18. C. Mas Arabí, A. Kudlinski, A. Mussot, and M. Conforti, "Geometric parametric instability in periodically modulated graded-index multimode fibers," Phys. Rev. A **97**(2), 023803 (2018).
19. Z. Deng, Y. Chen, J. Liu, C. Zhao, and D. Fan, "Correlation between geometric parametric instability sidebands in graded-index multimode fibers," Chaos **31**(1), 013109 (2021).
20. Z. Liu, L. G. Wright, D. N. Christodoulides, and F. W. Wise, "Kerr self-cleaning of femtosecond-pulsed beams in graded-index multimode fiber," Opt. Lett. **41**(16), 3675–3678 (2016).
21. K. Krupa, A. Tonello, B. M. Shalaby, M. Fabert, A. Barthélémy, G. Millot, S. Wabnitz, and V. Couderc, "Spatial beam self-cleaning in multimode fibres," Nat. Photonics **11**(4), 237–241 (2017).
22. L. G. Wright, S. Wabnitz, D. N. Christodoulides, and F. W. Wise, "Ultrabroadband Dispersive Radiation by Spatiotemporal Oscillation of Multimode Waves," Phys. Rev. Lett. **115**(22), 223902 (2015).
23. E. Nazemosadat, H. Pourbeyram, and A. Mafi, "Phase matching for spontaneous frequency conversion via four-wave mixing in graded-index multimode optical fibers," J. Opt. Soc. Am. B **33**(2), 144–150 (2016).
24. R. Dupiol, A. Bendahmane, K. Krupa, A. Tonello, M. Fabert, B. Kibler, T. Sylvestre, A. Barthelemy, V. Couderc, S. Wabnitz, and G. Millot, "Far-detuned cascaded intermodal four-wave mixing in a multimode fiber," Opt. Lett. **42**(7), 1293–1296 (2017).
25. H. E. Lopez-Aviles, F. O. Wu, Z. Sanjabi Eznaveh, M. A. Eftekhar, F. Wise, R. Amezcua Correa, and D. N. Christodoulides, "A systematic analysis of parametric instabilities in nonlinear parabolic multimode fibers," APL Photonics **4**(2), 022803 (2019).
26. A. Bendahmane, K. Krupa, A. Tonello, D. Modotto, T. Sylvestre, V. Couderc, S. Wabnitz, and G. Millot, "Seeded intermodal four-wave mixing in a highly multimode fiber," J. Opt. Soc. Am. B **35**(2), 295–301 (2018).
27. Y. Leventoux, G. Granger, A. Tonello, K. Krupa, G. Millot, S. Wabnitz, S. Février, and V. Couderc, "Experimental Evidence of the Real Multimode Nature of Geometric Parametric Instability," in *2020 Conference on Lasers and Electro-Optics (CLEO)*, (2020), pp. 1–2.
28. R. Dupiol, A. Bendahmane, K. Krupa, J. Fatome, A. Tonello, M. Fabert, V. Couderc, S. Wabnitz, and G. Millot, "Intermodal modulational instability in graded-index multimode optical fibers," Opt. Lett. **42**(17), 3419–3422 (2017).

Optics EXPRESS

29. M. Conforti, C. M. Arabi, A. Mussot, and A. Kudlinski, "Fast and accurate modeling of nonlinear pulse propagation in graded-index multimode fibers," Opt. Lett. **42**(19), 4004–4007 (2017).
30. F. Matera, A. Mecozzi, M. Romagnoli, and M. Settembre, "Sideband instability induced by periodic power variation in long-distance fiber links," Opt. Lett. **18**(18), 1499–1501 (1993).
31. K. Kikuchi, C. Lorattanasane, F. Futami, and S. Kaneko, "Observation of quasi-phase matched four-wave mixing assisted by periodic power variation in a long-distance optical amplifier chain," IEEE Photonics Technol. Lett. **7**(11), 1378–1380 (1995).
32. N. J. Smith and N. J. Doran, "Modulational instabilities in fibers with periodic dispersion management," Opt. Lett. **21**(8), 570–572 (1996).
33. J. C. Bronski and J. N. Kutz, "Modulational stability of plane waves in nonreturn-to-zero communications systems with dispersion management," Opt. Lett. **21**(13), 937–939 (1996).
34. M. Droques, A. Kudlinski, G. Bouwmans, G. Martinelli, and A. Mussot, "Experimental demonstration of modulation instability in an optical fiber with a periodic dispersion landscape," Opt. Lett. **37**(23), 4832–4834 (2012).
35. M. Droques, A. Kudlinski, G. Bouwmans, G. Martinelli, and A. Mussot, "Dynamics of the modulation instability spectrum in optical fibers with oscillating dispersion," Phys. Rev. A **87**(1), 013813 (2013).
36. A. Mussot, M. Conforti, S. Trillo, F. Copie, and A. Kudlinski, "Modulation instability in dispersion oscillating fibers," Adv. Opt. Photonics **10**(1), 1–42 (2018).
37. M. Droques, A. Kudlinski, G. Bouwmans, G. Martinelli, A. Mussot, A. Armaroli, and F. Biancalana, "Fourth-order dispersion mediated modulation instability in dispersion oscillating fibers," Opt. Lett. **38**(17), 3464–3467 (2013).
38. A. Kudlinski, A. Bendahmane, O. Vanvincq, C. M. Arabi, A. Mussot, and M. Conforti, "Impact of higher-order dispersion on geometric parametric instability in GRIN multimode fibers," in *CLEO Europe-EQEC*, (Munich, Germany, 2019).
39. I. H. Malitson, "Interspecimen Comparison of the Refractive Index of Fused Silica*, †," J. Opt. Soc. Am. **55**(10), 1205–1209 (1965).
40. J. W. Fleming, "Dispersion in GeO_2–SiO_2 glasses," Appl. Opt. **23**(24), 4486–4493 (1984).
41. K. Okamoto, *Fundamentals of Optical Waveguides - 2nd Edition* (San Diego Academic Press, 2006).
42. H. R. D. Sunak and S. P. Bastien, "Refractive index and material dispersion interpolation of doped silica in the 0.6-1.8 mu m wavelength region," IEEE Photonics Technol. Lett. **1**(6), 142–145 (1989).
43. T. Izawa and S. Sudo, *Optical Fibers: Materials and Fabrication*, Advances in Opto-Electronics (Springer, Netherlands, 1986).
44. S. A. V and T. M. Monro, "A full vectorial model for pulse propagation in emerging waveguides with subwavelength structures part I: Kerr nonlinearity," Opt. Express **17**(4), 2298–2318 (2009).
45. J. Hult, "A Fourth-Order Runge–Kutta in the Interaction Picture Method for Simulating Supercontinuum Generation in Optical Fibers," J. Lightwave Technol. **25**(12), 3770–3775 (2007).